This article has been accepted for publication in IEEE Access. This is the author's version which has not been fully edited and content may change prior to final publication. Citation information: DOI 10.1109/ACCESS.2026.3750743

IEEE Access
Multidisciplinary | Rapid Review | Open Access Journal

Date of publication xxxx 00, 0000, date of current version xxxx 00, 0000.

Digital Object Identifier sample-10.1109/ACCESS.year.0429000

STATISTICAL ANALYSIS OF RETINAL ARTERIAL NETWORKS: Graph-Based Radiomics Framework

OFÉLIO JORREIA[1], NUNO GONÇALVES[2], and RUI CORTESÃO[3]

[1] O. Jorreia is Ph.D student at the Department of Electrical and Computer Engineering – University of Coimbra, conducting research at the Institute of Systems and Robotics within the same university. Rua Silvio Lima – Polo II, Coimbra, PT 3030-290 (email: ofelio.jorreia@isr.uc.pt) .

[2] N. Gonçalves is researcher at the Institute of Systems and Robotics – University of Coimbra and Professor at the Dept. of Electrical and Computer Engineering of the University of Coimbra, Portugal (email:nunogon@deec.uc.pt).

[3] R. Cortesão is researcher at the Institute of Systems and Robotics – University of Coimbra and Professor at the Dept. of Electrical and Computer Engineering of the University of Coimbra, Portugal (email:cortesao@isr.uc.pt).

Corresponding author: Ofélio Jorreia (e-mail: ofelio.jorreia@isr.uc.pt).

Manuscript submitted to IEEE Access on October 12, 2026 and supported by Fundação para a Ciência e a Tecnologia (FCT) under reference grant PRT/BD/154310/2023 with DOI https://doi.org/10.54499/PRT/BD/154310/2023. This work was supported in part by Universidade Rovuma through a research fellowship awarded to Ofélio Jorreia.

ABSTRACT

Traditional radiomics enables mathematical and statistical analysis of medical images but remains limited in capturing the structural organization and complexity of vascular networks. This study analyzes the retinal arterial vasculature in relation to Cardiovascular Disease Risk (CVDR), using a graph-based radiomics framework, built on adjacency matrices derived from vascular graph representations. Images with near visible vasculature were selected from the Retinal Fundus Multi-disease Image Dataset (RFMiD) and Ocular Disease Intelligent Recognition (ODIR) dataset. Full MESSIDOR dataset was used reference. Shannon entropy values of $1.4 - 3.2$ bits, supported by Pearson correlation analysis, indicate substantial feature variability and suitability for machine learning (ML) applications. Six configurations (a gradient-boosted decision tree baseline, a metrics-only MLP, GAT and GCN alone, and each fused with the calculated metrics) are evaluated with respect to their discrimination performance. To improve model interpretability, explainable artificial intelligence (XAI) techniques, specifically SHAP (SHapley Additive exPlanations) and GNNExplainer, are employed to quantify the contribution of individual network metrics to model predictions. Results reveal the following contribution pattern: high Maximum degree consistently drives predictions toward higher CVDR risk, and high Diameter toward lower risk in RFMiD and MESSIDOR, whereas Global efficiency and Global clustering coefficient reverse direction across datasets. Only MESSIDOR shows a measurable signal, with smaller Diameter and higher Modularity in CVDR images and above-chance discrimination (AUC up to 0.62), while RFMiD and ODIR remain near chance.

INDEX TERMS Complex network metrics, explainability, graph-structured data, radiomics, retinal vasculature, statistical analysis.

I. INTRODUCTION

WITH the rapid growth of medical imaging data, traditional manual image interpretation is increasingly challenged in meeting clinical demands across diverse medical specialties [1]. Consequently, medical imaging has evolved from an auxiliary examination modality into a cornerstone of clinical diagnosis. Driven by this shift, automated medical image analysis techniques have advanced considerably, enabling more efficient, scalable, and objective diagnostic workflows [2]. Nevertheless, visual assessment remains susceptible to subjective bias, particularly when large volumes of visually similar images must be evaluated. To address these limitations, recent advances in computational technologies have accelerated the adoption of Deep Learning (DL), which has demonstrated remarkable accuracy in medical imaging and related fields [3]–[6]. Hence, DL has emerged as a key component of computer-aided diagnosis systems, improving both diagnostic accuracy and efficiency [7], [8]. Within this framework, radiomics has arisen as a prominent approach for the quantitative analysis of medical images, serving as an intermediate paradigm between traditional image analysis and end-to-end DL methods. This

This work is licensed under a Creative Commons Attribution 4.0 License. For more information, see https://creativecommons.org/licenses/by/4.0/

This article has been accepted for publication in IEEE Access. This is the author's version which has not been fully edited and
content may change prior to final publication. Citation information: DOI 10.1109/ACCESS.2026.3750743

manuscript proposes a graph-based radiomics approach for the analysis of retinal vascular networks, aimed at the early detection and screening of CVDR. Related study presented by Durante *et al.* [9] indicates hypertension-driven microvascular remodeling and vessel rarefaction lead to a reduction in both vessel density and wall elasticity, thereby increasing vascular resistance and promoting end-organ damage. According to referred study, over time, these alterations culminate in progressive vascular stiffening and functional decline, with clinically significant consequences across multiple organ systems, including the heart, kidneys, brain, and retina. This leads us to quantitatively characterize the topology of the vascular network, in the present case, the retinal vasculature. The manuscript presents the following main contributions within graph-based radiomics:

- Application of the novel graph-based radiomics framework proposed in [10] for the analysis of the retinal arterial network in CVDR screening. The investigated network metrics include Global efficiency, Maximum degree, Global clustering coefficient, Maximum closeness centrality, Diameter, and Modularity.
- Statistical interpretation of selected graph-based features for medical image analysis;
- Evaluation of the explainability of graph-based metrics as inputs into ML architectures.

The remainder of this manuscript is organized as follows: Section II presents the literature review, emphasizing the application of complex network analysis to medical imaging; The methodology and selected dataset are described in Section III. Section IV presents the corresponding statistical analysis, interpretation, and data-driven explainability; Finally, Section V presents the conclusions and outlines directions for future work.

II. RELATED WORKS

A. RADIOMIC DATA IN CLINICAL APPLICATIONS

Radiomics is a quantitative approach in medical imaging that extracts numerical features, known as radiomic features, from medical images such as Computed Tomography (CT), Magnetic Resonance Imaging (MRI), Positron Emission Tomography (PET), or ultrasound scans to reveal hidden patterns invisible to the human eye [11]–[13]. As an Artificial Intelligence (AI) assisted approach, it enables the extraction of quantitative information from medical images, providing additional objective data to support clinical analysis and decision-making [14]–[16]. Radiomics has achieved significant success in clinical applications, demonstrating its considerable potential to support diagnosis, prognosis, and treatment planning [17].

Radiomics features are commonly categorized into shape, statistical, texture, and transformed features. Shape features describe lesion geometry independent of intensity, while statistical features summarize voxel intensity distributions using histogram-based measures. Texture features characterize spatial gray-level patterns through matrices such as GLCM, GLRLM, GLSZM, NGTDM, and GLDM [18]. Transformed features are derived after applying filters or transformations, such as wavelet or Laplacian of Gaussian methods, to enhance complex image structures.

This study investigates graph-structured representations derived from the retinal vasculature to quantify topological and statistical properties relevant to vascular health assessment as novel radiomic features. Recently, network-based analysis of the organization principles, statistical properties and structures of the biological systems have been an active research topic. Image processing techniques, utilizing mesh-based representations, offer unique opportunities for advancing the analysis of medical data [19]–[22].

Furthermore, the study by Zare *et al.* [23] proposes a network-based framework for quantifying structural alterations in retinal vascular networks associated with diabetic retinopathy and glaucoma. In this study, the extracted graphs are characterized using network-based features, including the central node-distance distribution, central mean-weight distribution, and weighted degree distribution, while fractal dimensions [24], [25], are computed from both raw and skeletonized vessel maps. Jensen–Shannon divergence and Isomap-based nonlinear dimensionality reduction are subsequently employed to quantify and visualize structural differences between retinal groups and corresponding experimental results reveal statistically significant differences between healthy and pathological groups [23]. Meanwhile, Zhao *et al.* [22] propose a graph-based framework for reconstructing retinal vascular network topology and performing automatic artery/vein classification in color fundus images.

The retinal vasculature provides valuable biomarkers for the detection, assessment, and monitoring of various ocular and vascular diseases. It serves as a surrogate organ for assessing both ocular and systemic health [9]. Retinal examinations reveal not only eye-specific conditions but also early indicators of systemic diseases such as diabetes, hypertension, stroke, arteriosclerosis, cardiovascular, neurodegenerative, renal, and hepatic disorders [26]–[29].

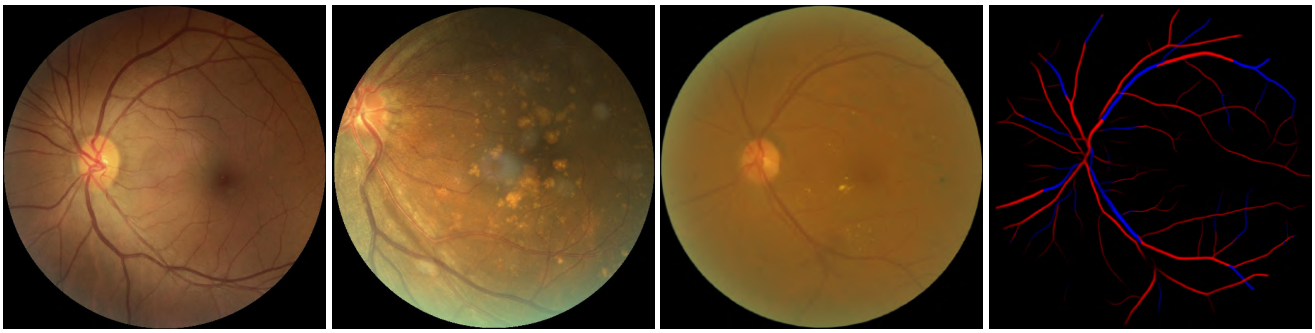
Existing vascular structure studies have largely been restricted to local descriptors, including tortuosity and bifurcation angles [30], [31]. This work extends conventional approaches by providing a global analysis of arterial network topology. Quantitative metrics are extracted from graph-based adjacency matrices representing the retinal vasculature using the complex-network analysis framework. The proposed methodology is currently undergoing further development, particularly in brain imaging research [32]–[36], and is herein extended to the analysis of vascular networks. The metrics selected in this study are grounded in complex network theory, as they collectively characterize topological network structure [21], [37]; in the present case, the objective is to characterize the arterial network specifically.

B. COMPLEX NETWORK METRICS

Complex network analysis is a powerful framework for studying systems characterized by numerous interacting compo-

This work is licensed under a Creative Commons Attribution 4.0 License. For more information, see https://creativecommons.org/licenses/by/4.0/

This article has been accepted for publication in IEEE Access. This is the author's version which has not been fully edited and
content may change prior to final publication. Citation information: DOI 10.1109/ACCESS.2026.3750743



(a) Clear selected fundus. (b) Fundus image with artifacts. (c) Blurry fundus image. (d) Segmentation errors of blurry fundus image 1c.

FIGURE 1: Sample of noisy fundus images from the ODIR dataset. These four images illustrate different artifacts and fundus conditions that make extraction of the vascular network difficult. The image in Fig. 1a is an example of the images selected from the ODIR dataset for this study.

nents, often represented as nodes connected by edges in a graph structure. Such networks are prevalent in various domains, including social networks, biological systems, and transportation infrastructures. The complexity and large scale of these networks pose significant challenges for analysis [38], requiring feature extraction to identify key nodes and substructures, as well as structural similarity measures to compare network topologies. These techniques facilitate the understanding of both local and global properties and the interactions among multiple network features, which are crucial for accurately characterizing real-world complex networks.

In recent years, complex network analysis has provided valuable insights into structural organization and dynamic processes, enabling applications ranging from epidemic modeling to transportation optimization [39]. The complex network metrics are essential for characterizing network topology, identifying key influential nodes, uncovering community structures, and elucidating overarching dynamics within diverse domains such as social [40], biological [41], and technological systems [42], [43]. In this study, they are applied to the retinal arterial network.

Aligning with Arakala et al. [44], the present study underscores the benefits of graph representation for vascular biometrics broadly, as well as the specific advantages of graph topology in matching vascular biometric graphs. The authors demonstrate that different types of small substructures dominate across distinct classes of vascular graphs, reflecting the way vasculature is structurally organized within the human body. Moreover, distance measures based on the number of vertices or edges within the maximum common subgraph are shown to discriminate significantly better between genuine and non-genuine comparisons than a simple count of matched vertices, as employed in iterative closest point (ICP)-based point-pattern matching.

The selected metrics and corresponding graph-based radiomic associations are listed as follows:

- *Global Efficiency* - measures the network's capacity to transfer blood between any pair of nodes, computed as the inverse of the shortest path lengths. A healthy vascular tree has evolved to optimize blood transport while minimizing energy expenditure, in accordance with Murray's law [45]. Accordingly, global efficiency reflects how effectively the network distributes peripheral blood flow.
- *Maximum Degree* - measures the highest number of connections (vessels) converging at a single node.
- *Global Clustering Coefficient* - measures the tendency of network nodes to form "triangles," or strongly interconnected local communities. Theoretically, the arterial network of the retina is a tree-like (dendritic) structure, characterized by low or zero local clustering [46].
- *Maximum Closeness Centrality* - measures how "close" the most central node is to all other nodes in the network, calculated as the inverse sum of the geodesic (shortest-path) distances. The node exhibiting maximum closeness centrality typically corresponds to the point of emergence of the central retinal artery, located near the optic disc.
- *Diameter* - defines the maximum extent of arterial perfusion, spanning from the optic disc to the extreme periphery of the retina.
- *Modularity* - reflects the extent to which the retina is organized into well-defined vascular arcades, each supplying a distinct territory with minimal overlap.

III. MATERIAL AND METHODS

This study used three publicly available datasets: RFMiD[1], ODIR[2] and MESSIDOR[3]. The retinal vascular structures are characterized from a network-theoretic perspective, and their associations with health-related anomalies. The ex-

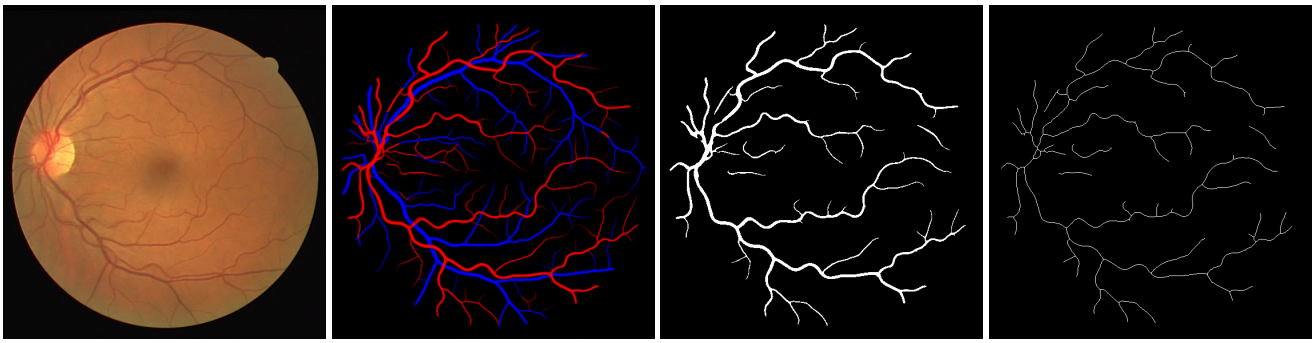
[1]https://pubmed.ncbi.nlm.nih.gov/39395210/ (PMID: 39395210, DOI: 10.1016/j.media.2024.103365).

[2]https://www.kaggle.com/datasets/andrewmvd/ocular-disease-recognition-odir5k

[3]https://www.kaggle.com/datasets/hanhan2010/messidor

This work is licensed under a Creative Commons Attribution 4.0 License. For more information, see https://creativecommons.org/licenses/by/4.0/

This article has been accepted for publication in IEEE Access. This is the author's version which has not been fully edited and
content may change prior to final publication. Citation information: DOI 10.1109/ACCESS.2026.3750743



(a) Sample RGB fundus. (b) SeqNet segmentation. (c) Arterial vasculature. (d) Arterial skeleton.

FIGURE 2: Segmentation of the eye vasculature for graph-structured data extraction. This exposes the arteries out of veins using the SeqNet [47] segmentation algorithm.

tracted metrics are analyzed for early quantitative screening of CVDR and used as input features for ML models.

From RFMiD and ODIR image selection was based on the dataset's descriptive metadata and the visual clarity of the vasculature under naked-eye assessment. Examination of CVDR-related descriptors aim to reveal that among images with clearly visible vasculature, the dataset includes individuals diagnosed with cardiovascular disease. This aligns with the study's main objective of quantitative assessment for early-detection screening by statistical analysis. The RFMiD dataset [48], [49], contains approximately 3200 high-resolution fundus images. Each sample consists of a JPEG retinal photograph organized to support supervised learning and the development of Computer-Aided Diagnosis (CAD) systems. Despite the high image resolution, in both RFMiD and ODIR datasets, many samples present pathological artifacts or lesions that obscure vascular structures (Fig. 1). An RGB filtering procedure was applied to reduce imaging artifacts without satisfactory results. Thus, 451 images were selected from the RFMiD dataset (training, validation, and test sets included), and 1458 images were selected from the ODIR dataset, all with clearly visible vasculature.

The MESSIDOR dataset is characterized by a clear exposure of the vasculature, therefore, all 1200 images with expert annotation were used, consistent with the study's exclusive focus on CVDR indicators associated with arterial blood pathways.

A. GRAPH REPRESENTATION OF VASCULAR NETWORK

To represent the retinal vascular network, segmented arterial images are represented as a planar arterial tree in which bifurcations and endpoints visible in fundus/OCTA images are defined as nodes and individual arterial segments as edges.

Segmentation is a challenging and important part of image analysis in this study [50], [51]. Even though a lot of algorithms for extraction and retinal vessel processing exist, there are still obstacles to producing the best output (Fig. 1d). With the rapid advancement of AI and DL technologies, this field has seen significant improvements in the accuracy and efficiency of segmenting anatomical structures and pathological areas from medical images [52], [53]. Zhou *et al.*'s [54] work aligns with that of Li *et al.* [47] in using DL for segmentation of the eye's vasculature. In their experiments, Li *et al.* propose a method for automatically analyzing retinal images for arterial and venous segmentation, as illustrated in Fig. 2. This method consists of two components: (i) A U-Net that segments vessels and classifies each pixel into artery and vein, coined SeqNet [47]; and (ii) post-processing to refine initial classification by SeqNet. We use this approach, to extract arteries from which we calculate complex network metrics. As shown by comparing Figures 1d and 2b, the quality of the segmented vasculature depends largely on the quality of the fundus image acquisition.

Algorithm 1: Graph-BRFExtract Algorithm

```
begin;
load images;
 /* loading image for coordinates extraction,
    SEs and target image in gray scale      */
detect and save T-points in a vector n;
define adjacency matrix W as square
  matrix with size n and zero elements;
                 // n is the number of T-points
for T-point i = 1 : n do
    for T-point j = 1 : n do
        for segment k = 1 : v do
            measure segment thickness k;
            // v is the number of vessel
               segments
            if T-point i, T-point j and segment k are
              connected then
                W_ij = w_ij
                /* where w_ij is corresponding to
                   v_k vessel thickness value   */
save matrix W;
end.
```

B. PROCESSING AND ANALYSIS PIPELINE

The proposed graph-based radiomics framework is composed of the following tasks and summarized in the radiomics

This work is licensed under a Creative Commons Attribution 4.0 License. For more information, see https://creativecommons.org/licenses/by/4.0/

This article has been accepted for publication in IEEE Access. This is the author's version which has not been fully edited and content may change prior to final publication. Citation information: DOI 10.1109/ACCESS.2026.3750743

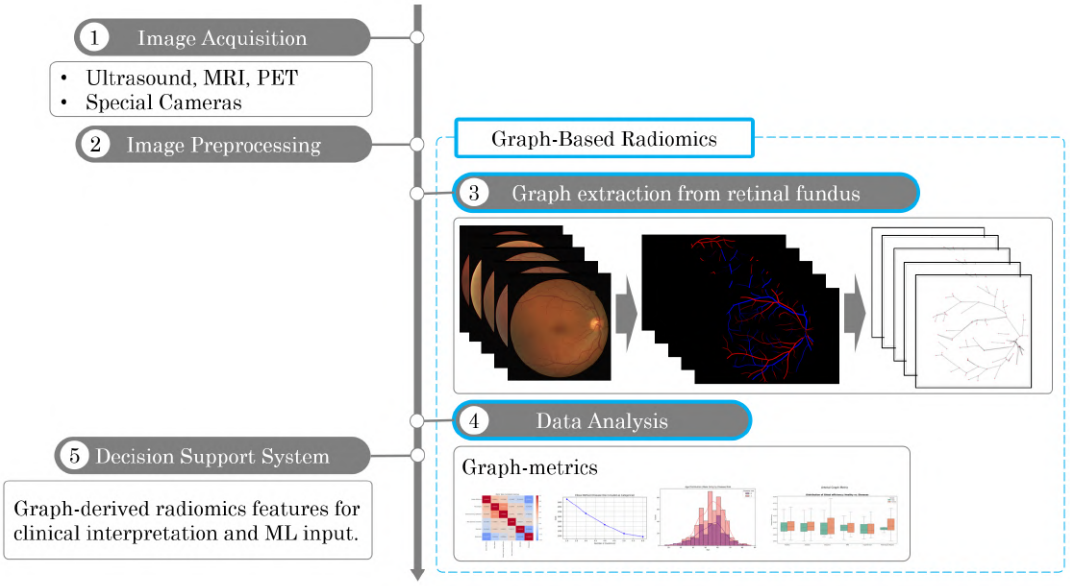


FIGURE 3: Graph-based radiomics pipeline: stages 1 and 2 correspond to conventional procedures commonly described in the radiomics literature [11], [14]. stage 3 performs the specific processing required for network feature extraction, whose outputs are subsequently used as inputs for stage 4. These two stages constitute the core contributions of the proposed graph-based radiomics framework. Finally, stage 5 adapts the explainability and interpretation procedures described in the literature to the specific context of retinal vascular network analysis considered in this study.

pipeline shown in Fig. 3. In the sequence, graph extraction and metric computation are performed using the MATLAB R2025a toolbox, while statistical analysis, including the explainability evaluation stage, is conducted using Python (version 3.12.11):

1) **Graph extraction from retinal fundus** - this is performed using a segmented binary arterial image as input within stage 3 of the pipeline. Centerline and junction are calculated to obtain the arterial skeleton. Vessel segments, branching points, and terminal nodes are then identified to construct an artery-only graph preserving the anatomical topology of retinal circulation. In this work we propose Algorithm 1: Graph-BRFExtract Algorithm[4], which is an updated version of Graph-BRFExtract Algorithm proposed in [10] since bifurcation identification is not required, as the segmentation process directly yields the arterial network. The resulting connectivity is represented by an adjacency matrix whose edge weights encode the distance-transform-based thickness of each vascular segment (Fig. 4).
2) **Calculation of graph-based metrics from the adjacency matrix** - from the generated graph representation, in stage 4 of the pipeline, several complex-network metrics can be computed. In this work, scalar metrics potentially associated with retinal arterial blood flow are selected. Specifically, **global efficiency** is defined as the average inverse shortest path length between node pairs and interpreted as an indicator of the network's ability to efficiently deliver blood to distal regions. The **clustering coefficient** quantifies local connectivity and is used as a measure of regional redundancy and collateral robustness. Characteristic path length captures

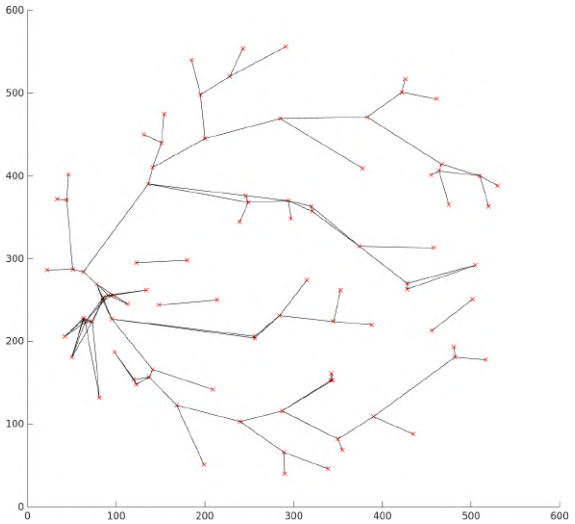


FIGURE 4: Arterial graph reconstructed from its adjacency matrix. This figure shows nodes and edges forming triangular substructures, from which the Global clustering coefficient is computed. As the arterial network is expected to exhibit a predominantly tree-like (dendritic) topology, this value should theoretically approach zero.

[4]https://github.com/ofelio-jorreia/Graph-BRFExtract-Algorithm/tree/main

This work is licensed under a Creative Commons Attribution 4.0 License. For more information, see https://creativecommons.org/licenses/by/4.0/

This article has been accepted for publication in IEEE Access. This is the author's version which has not been fully edited and
content may change prior to final publication. Citation information: DOI 10.1109/ACCESS.2026.3750743

global integration of the arterial tree, with larger values indicating increased structural fragmentation. In addition, **degree** and **centrality-based measures** are derived to identify highly connected arterial hubs and critical branching points, thereby linking the graph representation to clinically meaningful indicators of vascular vulnerability, hemodynamic load, and perfusion efficiency [21], [37], [55], [56]. **Graph diameter** is defined as the maximum geodesic distance between any pair of nodes in the network, representing the longest shortest path and characterizing the upper bound of spatial dispersion and traversal cost across the arterial tree. In contrast, **graph modularity** quantifies the strength of the network's community structure by comparing the density of intra-cluster edges to that expected under a random null model, thereby identifying functionally cohesive subregions with dense internal connectivity and sparse interconnections.Together, these metrics provide a comprehensive assessment of arterial network organization and resilience. Specifically, a lower diameter indicates improved global accessibility, whereas higher modularity reflects a more decentralized and compartmentalized topology, potentially supporting localized blood flow regulation.

3) **Statistical analysis of the graph-based metrics** -The computed metrics are subsequently subjected to statistical analysis. Initially, characterization and descriptive statistics, including mean, median, and standard deviation, are performed. Thereafter, the graph-derived metrics are analyzed for abnormality screening and CVDR assessment. The employed statistical methods include Pearson correlation analysis and Shannon entropy. Pearson correlation analysis is used to identify redundant features, and Shannon entropy is applied to quantify how much information each feature provides about the class label. This step is likewise incorporated into stage 4 of the proposed pipeline. This statistical analysis may support feature selection and contribute to improving the accuracy of ML models.
4) **Data-driven explainability** - finally, Stage 5 requires clinical expert interpretation alongside explainability analysis to assess the contribution of each metric both to the patient's vascular status within the proposed radiomics framework and to the ML model's predictions.

IV. EXPERIMENTS

After SeqNet segmentation, which involves separating the arterial and venous vasculature, the arterial network is divided into individual segments. The thickness of each segment is measured as the max euclidean distance between the middle segment pixel, corresponding to its skeleton pixel, and its borders. The computed value is represented as weight between adjacent nodes in the corresponding adjacency matrix use for arterial graph reconstruction (Alg. 1). The euclidean distance D is calculated using the following equation, through distance transform function in MatLab-R2025a toolbox:

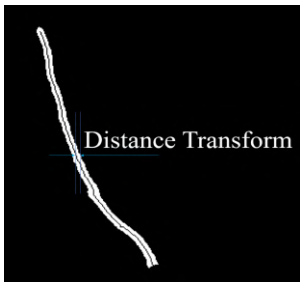
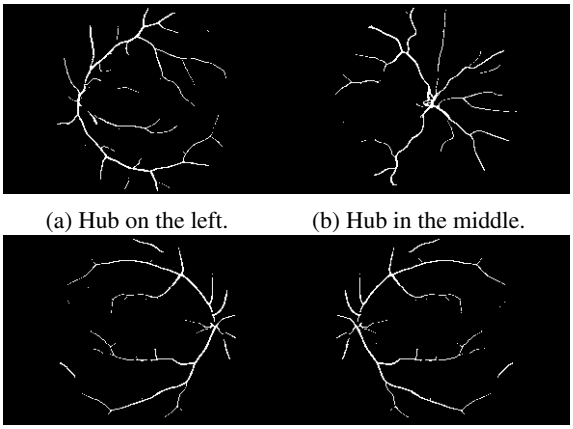


FIGURE 5: Distance-transform computation between vessel skeleton pixels and the vessel boundary in a sample arterial segment.



(a) Hub on the left. (b) Hub in the middle. (c) Hub on the right. (d) Hub on the right flipped horizontally as horizontal mirroring.

FIGURE 6: Location of the hub node in retinal images. The highlighted regions indicate the position of the most connected node (hub) within the arterial network.

$$D(x,y) = \max_{(i,j)\,:\,B(i,j)=0} \sqrt{(x-i)^2 + (y-j)^2} \qquad (1)$$

That is, for each pixel (x,y), $D(x,y)$ is the Euclidean distance to the nearest background pixel (i,j) with $B(i,j) = 0$. Fig. 5 illustrates the distance transform measurement used to estimate vessel thickness from the skeleton to the vessel boundary.

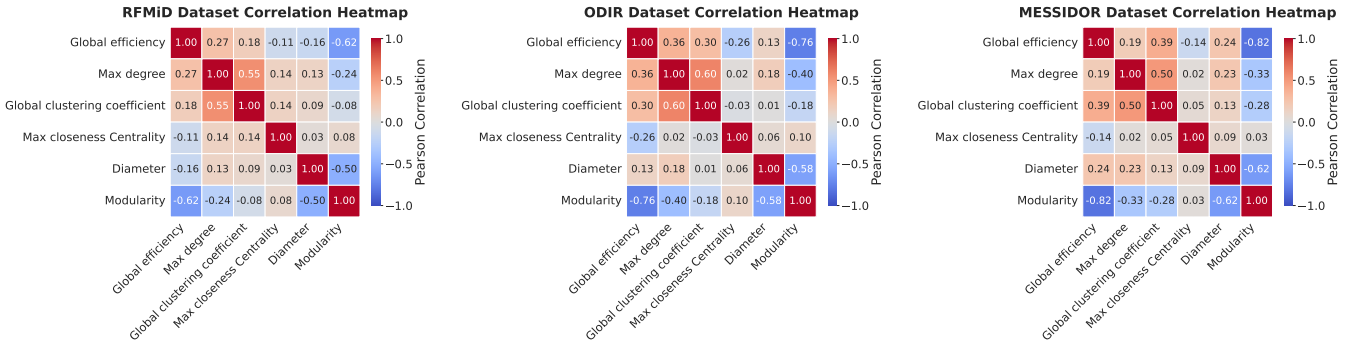
From the selected images in RFMiD, three visual categories can be identified based on the location of the most densely connected node within the vascular graph – the hub node in Fig. 6. The first two categories correspond to images whose dominant connectivity region appears on the left or right side; these can be interpreted equivalently, as they become similarly oriented under horizontal flipping. A third category consists of images in which the most connected node is located in the middle region of the image. This latter configuration exhibits a distinct structural organization and, therefore, its corresponding graph metrics require a separate interpretation.

This work is licensed under a Creative Commons Attribution 4.0 License. For more information, see https://creativecommons.org/licenses/by/4.0/

This article has been accepted for publication in IEEE Access. This is the author's version which has not been fully edited and
content may change prior to final publication. Citation information: DOI 10.1109/ACCESS.2026.3750743

TABLE 1: Descriptive statistics grouped by CVDR, including the mean, median, and standard deviation computed from the graph vascular representation of arterial images, in the RFMiD, ODIR, and MESSIDOR datasets.

		RFMiD			ODIR			MESSIDOR		
CVDR	**Metric**	**Mean**	**Median**	**Std Dev**	**Mean**	**Median**	**Std Dev**	**Mean**	**Median**	**Std Dev**
1	Global efficiency	0.033	0.031	0.014	0.082	0.078	0.031	0.055	0.051	0.025
	Max degree	5.997	6.000	1.281	6.525	6.000	2.295	14.639	13.386	5.245
	Global clustering coefficient	0.171	0.175	0.059	0.209	0.209	0.090	0.132	0.124	0.076
	Max closeness Centrality	0.830	1.000	0.247	0.907	1.000	0.161	0.883	1.000	0.169
	Diameter	75.439	73.547	22.124	20.399	20.837	6.605	26.759	26.211	8.716
	Modularity	0.471	0.465	0.187	0.454	0.451	0.216	0.525	0.543	0.211
0	Global efficiency	0.032	0.029	0.012	0.086	0.082	0.032	0.055	0.053	0.020
	Max degree	5.985	6.000	1.473	6.574	6.000	2.343	14.174	13.244	4.598
	Global clustering coefficient	0.174	0.179	0.064	0.213	0.211	0.087	0.122	0.121	0.064
	Max closeness Centrality	0.802	1.000	0.255	0.895	1.000	0.175	0.891	1.000	0.158
	Diameter	78.113	77.842	22.952	20.696	20.893	7.056	30.354	29.613	8.879
	Modularity	0.479	0.485	0.189	0.434	0.431	0.216	0.474	0.466	0.199



(a) RFMiD (b) ODIR (c) MESSIDOR

FIGURE 7: Pairwise Pearson correlation heatmaps illustrating the relationships among graph-based network metrics.

In this study, the statistical analysis of the extracted features is performed with respect to CVDR variable, which is defined as the classification target or clustering group.

TABLE 2: Shannon entropy values of the network metrics and of CVDR status (in bits) calculated in the RFMiD, ODIR, and MESSIDOR datasets.

Metric	**RFMiD**	**ODIR**	**MESSIDOR**
Global efficiency	2.496	1.872	2.427
Max degree	2.412	1.861	2.305
Global clustering coefficient	2.768	2.558	2.501
Max closeness Centrality	1.447	1.509	1.556
Diameter	2.752	2.753	2.669
Modularity	3.080	3.180	3.139
CVDR status	0.970	0.929	0.995

Retinal images whose arterial vasculature indicates a risk of disease (CVDR) are labeled as 1, whereas those without such indication are labeled as 0. For clarity and interpretability, the target class in the ODIR dataset was reformulated from "normal (healthy)", represented by the label "N" in the dataset's annotation CSV file, to "CVDR." The corresponding class labels were remapped accordingly: the "normal" class was recoded from 1 to 0, and, correspondingly, the opposing class was recoded from 0 to 1. Regarding the MESSIDOR dataset, the disease-risk classes were merged into a single class.

Shannon entropy [59], [60] is used to detect nonlinearity presenting the average uncertainty or information content of a random variable x, expressed in bits when using base-2 logarithms. It is calculated as:

$$H(X) = -\sum_{i=1}^{n} p(x_i)\ \log_2 p(x_i) \tag{2}$$

where $H(X)$ represents the average amount of information, surprise, or uncertainty inherent in the variable's possible outcomes and represents the minimum average number of bits needed to encode data, with higher entropy indicating greater unpredictability. As shown in Table 2, the majority of the graph-based metrics exhibit Shannon entropy values exceeding 2 bits, indicating a relatively high degree of variability within the data, whereas CVDR status exhibits lower entropy (0.970 bits in RFMiD, 0.929 bits in ODIR and 0.995 bits in MESSIDOR), close to the theoretical 1 bit for a binary variable and reflecting the moderate class imbalance across the three datasets.

Pearson correlation [61] is employed to quantify the strength and direction of the linear relationship between pairwise numeric variables. The Fig. 7 illustrates correlation

This work is licensed under a Creative Commons Attribution 4.0 License. For more information, see https://creativecommons.org/licenses/by/4.0/

This article has been accepted for publication in IEEE Access. This is the author's version which has not been fully edited and
content may change prior to final publication. Citation information: DOI 10.1109/ACCESS.2026.3750743

TABLE 3: Welch's *t*-test results comparing metric means between datasets, overall and stratified by CVDR status, with Holm-Bonferroni adjusted *p*-values ($\alpha = 0.05$) and Hedges' g effect sizes. Positive g indicates a higher mean in the first-named dataset. * indicates significance after adjustment. Effect size: negligible ($|g| < 0.2$), small (0.2–0.5), medium (0.5–0.8), large (> 0.8).

	between datasets		CVDR=1		CVDR=0	
	p_{adj}	g	p_{adj}	g	p_{adj}	g
ODIR vs RFMiD						
Global efficiency	$< 10^{-300}{}^*$	1.81	$5.03 \times 10^{-200}{}^*$	1.73	$7.13 \times 10^{-141}{}^*$	1.95
Max degree	$2.50 \times 10^{-9}{}^*$	0.26	$5.68 \times 10^{-6}{}^*$	0.25	$5.07 \times 10^{-4}{}^*$	0.28
Global clustering coefficient	$2.59 \times 10^{-24}{}^*$	0.46	$1.42 \times 10^{-15}{}^*$	0.46	$1.40 \times 10^{-9}{}^*$	0.49
Max closeness centrality	$1.13 \times 10^{-10}{}^*$	0.44	$5.68 \times 10^{-6}{}^*$	0.42	$3.49 \times 10^{-5}{}^*$	0.46
Diameter	$3.45 \times 10^{-214}{}^*$	−4.41	$8.01 \times 10^{-129}{}^*$	−4.52	$4.78 \times 10^{-86}{}^*$	−4.25
Modularity	$3.67 \times 10^{-2}{}^*$	−0.13	0.625	−0.08	$3.54 \times 10^{-2}{}^*$	−0.22
MESSIDOR vs RFMiD						
Global efficiency	$2.38 \times 10^{-117}{}^*$	1.11	$6.80 \times 10^{-57}{}^*$	1.00	$3.50 \times 10^{-63}{}^*$	1.28
Max degree	$< 10^{-300}{}^*$	1.99	$9.25 \times 10^{-186}{}^*$	1.96	$1.15 \times 10^{-165}{}^*$	2.04
Global clustering coefficient	$5.68 \times 10^{-35}{}^*$	−0.66	$5.93 \times 10^{-16}{}^*$	−0.55	$8.69 \times 10^{-19}{}^*$	−0.81
Max closeness centrality	$4.61 \times 10^{-7}{}^*$	0.35	$4.80 \times 10^{-3}{}^*$	0.27	$6.40 \times 10^{-5}{}^*$	0.47
Diameter	$6.61 \times 10^{-189}{}^*$	−3.36	$1.65 \times 10^{-117}{}^*$	−3.39	$5.83 \times 10^{-73}{}^*$	−3.40
Modularity	$3.39 \times 10^{-2}{}^*$	0.14	$5.00 \times 10^{-4}{}^*$	0.27	1.000	−0.03
MESSIDOR vs ODIR						
Global efficiency	$7.75 \times 10^{-138}{}^*$	−1.01	$2.38 \times 10^{-73}{}^*$	−0.94	$2.25 \times 10^{-62}{}^*$	−1.15
Max degree	$< 10^{-300}{}^*$	2.11	$2.38 \times 10^{-173}{}^*$	2.15	$2.12 \times 10^{-157}{}^*$	2.06
Global clustering coefficient	$1.22 \times 10^{-138}{}^*$	−1.02	$1.00 \times 10^{-67}{}^*$	−0.91	$1.75 \times 10^{-68}{}^*$	−1.20
Max closeness centrality	$3.77 \times 10^{-2}{}^*$	−0.10	$1.77 \times 10^{-2}{}^*$	−0.15	1.000	−0.03
Diameter	$1.00 \times 10^{-120}{}^*$	1.01	$2.96 \times 10^{-49}{}^*$	0.85	$2.88 \times 10^{-71}{}^*$	1.20
Modularity	$5.54 \times 10^{-10}{}^*$	0.26	$7.71 \times 10^{-10}{}^*$	0.33	$1.30 \times 10^{-2}{}^*$	0.19

TABLE 4: Welch's *t*-test results comparing metric means between CVDR groups within each dataset, with Holm-Bonferroni adjusted *p*-values ($\alpha = 0.05$) and Hedges' g effect sizes. Positive g indicates a higher mean in the CVDR=1 group. * indicates significance after adjustment. Effect size: negligible ($|g| < 0.2$), small (0.2–0.5), medium (0.5–0.8), large (> 0.8).

	CVDR, within ODIR		CVDR, within RFMiD		CVDR, within MESSIDOR	
	p_{adj}	g	p_{adj}	g	p_{adj}	g
Global efficiency	0.658	−0.11	1.000	0.11	1.000	−0.01
Max degree	1.000	−0.02	1.000	0.01	1.000	0.09
Global clustering coefficient	1.000	−0.05	1.000	−0.05	0.227	0.14
Max closeness centrality	1.000	0.07	1.000	0.11	1.000	−0.05
Diameter	1.000	−0.04	1.000	−0.12	$9.09 \times 10^{-11}{}^*$	−0.41
Modularity	1.000	0.09	1.000	−0.05	$3.42 \times 10^{-4}{}^*$	0.25

heatmaps for each dataset, highlighting both positive and negative correlations among metrics.

Welch's *t*-tests [62] were performed to compare metric means (i) between datasets, overall and stratified by CVDR status, across all three pairwise dataset combinations (Table 3), and (ii) between CVDR groups, separately within each of the three datasets (Table 4). Holm-Bonferroni correction [63] was applied within each family (18 tests per pairwise dataset comparison; 18 CVDR-related tests across the three datasets), using a conservative family size of 20 tests, and Hedges' g [64] is reported as the effect size.

Nearly all dataset-related comparisons remained significant after correction, with three exceptions: Modularity within the CVDR=1 subgroup for ODIR vs. RFMiD ($p_{\text{adj}} = 0.625$), Modularity within the CVDR=0 subgroup for MESSIDOR vs. RFMiD ($p_{\text{adj}} = 1.000$), and Max closeness centrality within the CVDR=0 subgroup for MESSIDOR vs. ODIR ($p_{\text{adj}} = 1.000$). Effect sizes ranged from negligible (Modularity, Max closeness centrality) to very large: Diameter, $|g| \geq 3.36$ in both comparisons against RFMiD and $0.85 \leq |g| \leq 1.20$ for MESSIDOR vs. ODIR; Global efficiency, $|g| > 0.9$ across all three pairs. Notably, the MESSIDOR reveals that Max degree and Global clustering coefficient reach large effect size. This indicates that most graph-based metrics are highly sensitive to differences in image acquisition and resolution across the three data sources.

In contrast, within-dataset CVDR comparisons showed no significant effect for any metric in ODIR or RFMiD

This work is licensed under a Creative Commons Attribution 4.0 License. For more information, see https://creativecommons.org/licenses/by/4.0/

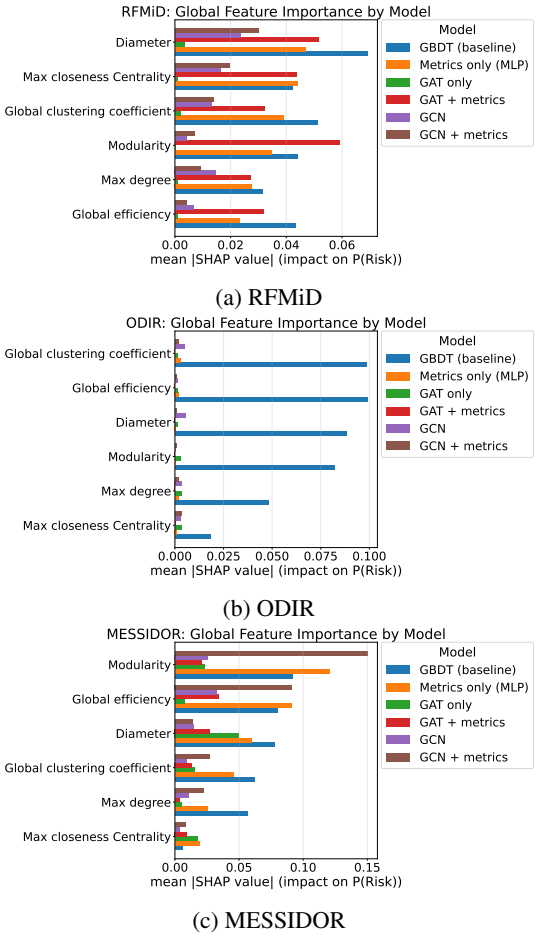
This article has been accepted for publication in IEEE Access. This is the author's version which has not been fully edited and
content may change prior to final publication. Citation information: DOI 10.1109/ACCESS.2026.3750743

($p_{\text{adj}} \geq 0.658$; $|g| \leq 0.12$ throughout). Within MESSIDOR, however, Diameter ($p_{\text{adj}} = 9.09 \times 10^{-11}$, $g = -0.41$) and Modularity ($p_{\text{adj}} = 3.42 \times 10^{-4}$, $g = 0.25$) showed statistically significant, small-magnitude differences between CVDR groups, while the remaining four metrics were non-significant ($|g| \leq 0.14$).

A. STATISTICAL DISCUSSION

Table 1 provide the descriptive statistics of the network metrics, while Tables 3 and 4 reveal subtle yet measurable topological changes in arterial networks associated with CVDR status across the three datasets, summarized as follows:

- **Network Integration and Global Structure** - CVDR networks exhibit a smaller diameter than non-risk networks in all three datasets: RFMiD (75.44 vs. 78.11), ODIR (20.40 vs. 20.70), and MESSIDOR (26.76 vs. 30.35). The difference is significant only in MESSIDOR ($p_{\text{adj}} < 10^{-10}$, $g = -0.41$), suggesting marginally more compact global integration in disease-affected networks. Global efficiency shows no consistent direction: slightly higher in the risk group in RFMiD (0.033 vs. 0.032), slightly lower in ODIR (0.082 vs. 0.086), and equal in MESSIDOR (0.055 vs. 0.055), with no significant within-dataset effect. The differing diameter ranges between datasets mainly reflect differences in input image resolution (2144×1424 pxl for RFMiD, 512×512 pxl for ODIR and 800×800 pxl for MESSIDOR), so resolution effects must be considered when interpreting these metrics.
- **Community Structure and Clustering** - Modularity is marginally lower in the CVDR group in RFMiD (0.471 vs. 0.479) but higher in ODIR (0.454 vs. 0.434) and MESSIDOR (0.525 vs. 0.474). Only the MESSIDOR difference is significant ($p_{\text{adj}} = 3.42 \times 10^{-4}$, $g = 0.25$). The global clustering coefficient is slightly lower in CVDR cases in RFMiD (0.171 vs. 0.174) and ODIR (0.209 vs. 0.213) but slightly higher in MESSIDOR (0.132 vs. 0.122), with no significant within-dataset effect. In all groups the values are nonzero, which indicates triangular artifacts arising from graph reconstruction, since a tree-like arterial network should have a clustering coefficient close to zero (Fig. 4).
- **Node Centrality and Connectivity** - Maximum degree is stable between CVDR groups within each dataset (RFMiD: 5.997 vs. 5.985; ODIR: 6.525 vs. 6.574; MESSIDOR: 14.639 vs. 14.174; $|g| \leq 0.09$, $p_{\text{adj}} = 1.000$). Its absolute level, however, differs markedly between datasets (approximately 6.0 for RFMiD, 6.5 for ODIR, and 14.4 for MESSIDOR), consistent with acquisition differences. Maximum closeness centrality is slightly higher in the CVDR group in RFMiD (0.830 vs. 0.802) and ODIR (0.907 vs. 0.895) but slightly lower in MESSIDOR (0.883 vs. 0.891). None of these differences is significant ($|g| \leq 0.11$).



(a) RFMiD

(b) ODIR

(c) MESSIDOR

FIGURE 8: Global feature importance, measured as mean |SHAP| on the predicted risk probability, of the six graph-level metrics with GBDT baseline across models in RFMiD (a), ODIR (b), and MESSIDOR (c).

B. MODEL ARCHITECTURE AND EXPLAINABILITY

In machine learning, SHAP and GNNExplainer are post-hoc explanation framework that decomposes closed-box model predictions into additive feature contributions, thereby enhancing explainability and bridging the gap between model outputs and human-interpretable reasoning [65].

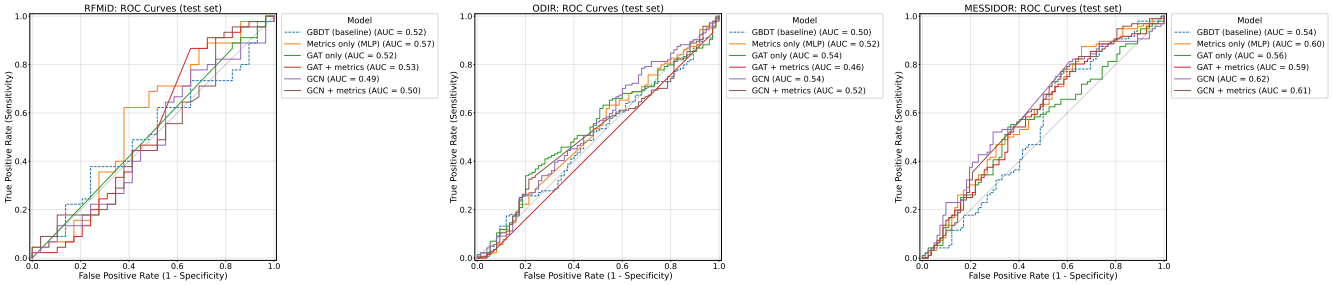
To obtain explainable representations, a Graph Neural Network (GNN) model is trained. Among the available GNN architectures, the Graph Attention Network (GAT) is selected for its ability to effectively capture the topological characteristics of the retinal vascular network [66]–[68]. In particular, the attention mechanism enables the model to learn relationships between parent vessels and their corresponding downstream branches [69], [70]. Through multiple graph-attention layers, information propagates from the principal retinal arteries toward smaller vascular structures, enabling the model to determine whether local vascular alterations correspond to isolated events or to broader systemic vascular abnormalities. Training results are presented in Table 5. The interpretation of the results primarily emphasizes the

This work is licensed under a Creative Commons Attribution 4.0 License. For more information, see https://creativecommons.org/licenses/by/4.0/

This article has been accepted for publication in IEEE Access. This is the author's version which has not been fully edited and
content may change prior to final publication. Citation information: DOI 10.1109/ACCESS.2026.3750743

TABLE 5: Comparative configuration analysis on the held-out test set of a stratified 70/15/15 train/validation/test split (decision threshold 0.5). F_1-score(Risk) and AUC are reported with 95% CI. * indicates that the AUC interval lies entirely above chance level (0.50); † indicates that it lies entirely below. The majority-class baseline is the accuracy obtained by always predicting the Risk class on the test set.

Dataset	Configuration	Accuracy	Precision	Recall	Specificity	F_1-score(Risk) [95% CI]	AUC [95% CI]
RFMiD $n = 451$ $n_{\text{test}} = 74$	GBDT (baseline)	0.50	0.61	0.51	0.48	0.55 [0.41, 0.68]	0.52 [0.39, 0.65]
	Metrics only (MLP)	0.61	0.65	0.78	0.34	0.71 [0.60, 0.80]	0.57 [0.43, 0.71]
	GAT only	0.61	0.63	0.89	0.17	0.73 [0.62, 0.82]	0.52 [0.44, 0.61]
	GAT + metrics	0.64	0.65	0.87	0.28	0.74 [0.64, 0.83]	0.53 [0.37, 0.66]
	GCN	0.59	0.64	0.78	0.31	0.70 [0.58, 0.79]	0.49 [0.35, 0.63]
	GCN + metrics	0.64	0.64	0.93	0.17	0.76 [0.65, 0.84]	0.50 [0.37, 0.64]
Majority-class baseline: accuracy 0.61							
ODIR $n = 1458$ ($n_{\text{test}} = 219$)	GBDT (baseline)	0.56	0.66	0.69	0.31	0.68 [0.61, 0.74]	0.50 [0.41, 0.57]
	Metrics only (MLP)	0.65	0.66	0.99	0.01	0.79 [0.74, 0.83]	0.52 [0.44, 0.61]
	GAT only	0.63	0.65	0.95	0.01	0.77 [0.72, 0.82]	0.54 [0.46, 0.62]
	GAT + metrics	0.65	0.66	0.99	0.00	0.79 [0.74, 0.83]	0.46 [0.43, 0.50]†
	GCN	0.65	0.66	0.98	0.03	0.79 [0.74, 0.83]	0.54 [0.46, 0.62]
	GCN + metrics	0.64	0.65	0.98	0.00	0.78 [0.73, 0.83]	0.52 [0.43, 0.60]
Majority-class baseline: accuracy 0.66							
MESSIDOR $n = 1181$ $n_{\text{test}} = 178$	GBDT (baseline)	0.49	0.53	0.47	0.51	0.50 [0.40, 0.58]	0.54 [0.46, 0.63]
	Metrics only (MLP)	0.57	0.60	0.57	0.56	0.59 [0.50, 0.67]	0.60 [0.52, 0.69]*
	GAT only	0.53	0.54	0.82	0.20	0.66 [0.59, 0.72]	0.56 [0.48, 0.65]
	GAT + metrics	0.56	0.56	0.93	0.13	0.70 [0.63, 0.75]	0.59 [0.50, 0.67]*
	GCN	0.60	0.58	0.89	0.26	0.70 [0.63, 0.76]	0.62 [0.54, 0.70]*
	GCN + metrics	0.59	0.61	0.68	0.49	0.64 [0.56, 0.71]	0.61 [0.52, 0.70]*
Majority-class baseline: accuracy 0.54							



(a) RFMiD (b) ODIR (c) MESSIDOR

FIGURE 9: ROC curves on the held-out test set for the six configurations in RFMiD (a), ODIR (b), and MESSIDOR (c), with the AUC of each model shown in the legend. In RFMiD and ODIR, all curves lie close to the diagonal (AUC 0.46–0.57). In MESSIDOR, all models lie above chance (AUC 0.54–0.62). Confidence intervals for each AUC are reported in Table 5.

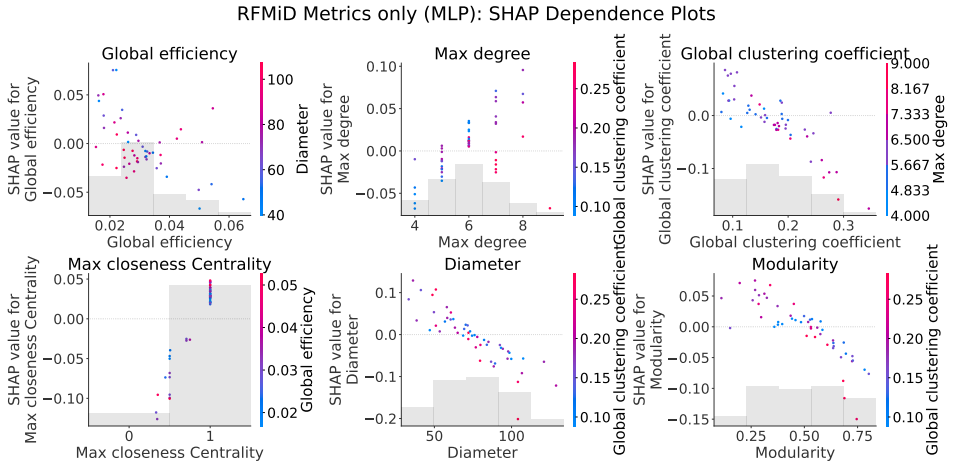
F_1-score metric, given the class imbalance observed in two datasets: RFMiD and ODIR.

- ***Configuration Design*** – To assess whether graph structure adds discriminative value beyond aggregate descriptors, six configurations were compared under a common protocol, with a gradient-boosted decision tree (GBDT) trained on the computed graph metrics as the baseline:
  - GBDT (baseline), applied to the computed graph metrics;
  - computed graph metrics alone, using a multilayer perceptron (MLP);
  - GAT structure alone;
  - GAT structure fused with the computed graph metrics (GAT + metrics);
  - GCN structure alone, as an architectural control for the GAT;
  - GCN structure fused with the computed graph metrics (GCN + metrics).

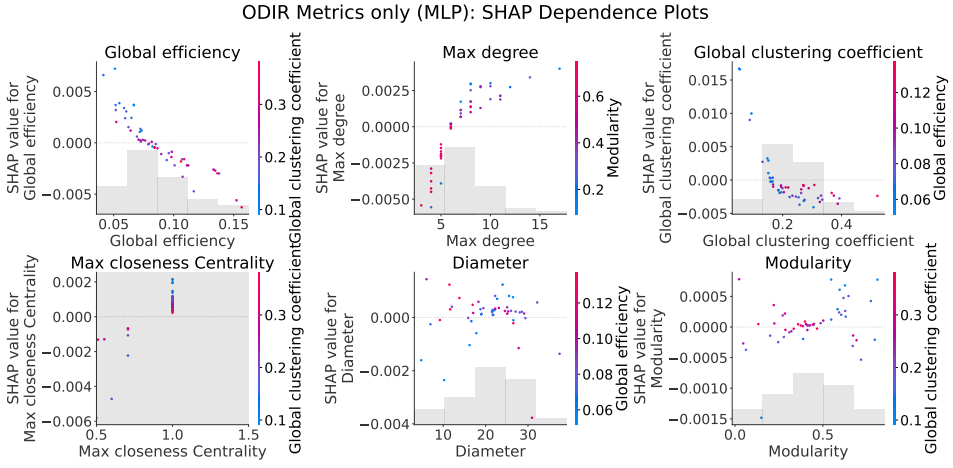
The GCN replaces the GAT attention mechanism with uniform neighborhood aggregation, while node features and the stratified $70/15/15$ train/validation/test split remain unchanged. Hyperparameters were selected by grid search based on the validation F_1-score (Risk), and all results were evaluated on the held-out test set using a decision threshold of 0.5 (Table 5). RFMiD represents a small-sample setting, ODIR a setting characterized by

This work is licensed under a Creative Commons Attribution 4.0 License. For more information, see https://creativecommons.org/licenses/by/4.0/

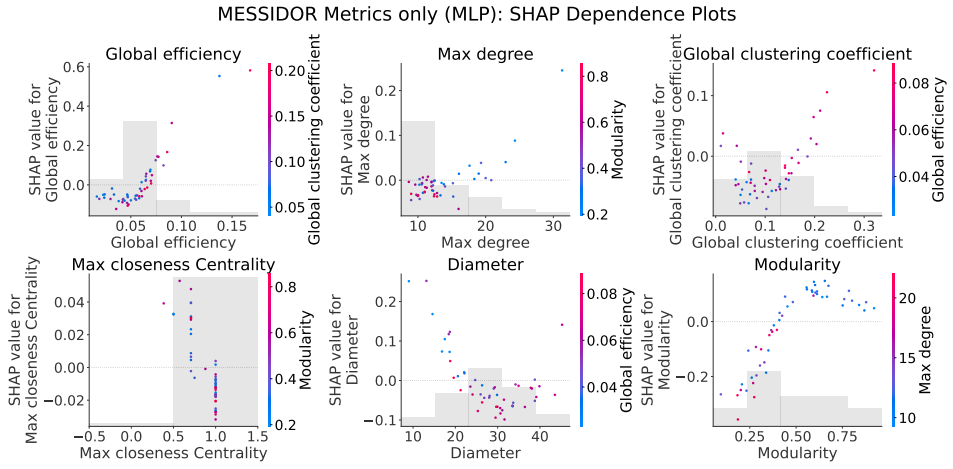
This article has been accepted for publication in IEEE Access. This is the author's version which has not been fully edited and
content may change prior to final publication. Citation information: DOI 10.1109/ACCESS.2026.3750743



(a) RFMiD, metrics-only (MLP)



(b) ODIR, metrics-only (MLP)



(c) MESSIDOR, metrics-only (MLP)

FIGURE 10: SHAP dependence plots of the six graph-level metrics, showing the impact on the predicted risk probability. Colour encodes the interacting metric and the grey histograms show the distribution of each metric. In RFMiD (a), higher diameter, modularity, and clustering coefficient lower the predicted risk, whereas a maximum closeness centrality of 1 raises it. In MESSIDOR (c), lower diameter and higher modularity, clustering coefficient, and global efficiency raise the predicted risk. In ODIR (b), SHAP values do not exceed 0.02, one to two orders of magnitude smaller than in the other datasets, and are therefore negligible.

This work is licensed under a Creative Commons Attribution 4.0 License. For more information, see https://creativecommons.org/licenses/by/4.0/

This article has been accepted for publication in IEEE Access. This is the author's version which has not been fully edited and
content may change prior to final publication. Citation information: DOI 10.1109/ACCESS.2026.3750743

noisy fundus images, and MESSIDOR a clean, full-scale baseline dataset. All neural configurations exceeded the GBDT baseline in F_1-score (Risk), with ΔF_1 ranging from 0.09 to 0.21. However, in RFMiD and ODIR, the high F_1-scores primarily reflect high recall at near-zero specificity. Moreover, no ODIR configuration exceeded the majority-class accuracy of 0.66. Thus, AUC provides a more informative measure of discriminative performance, notably, the ODIR GAT + metrics model remains below chance.

In the clean MESSIDOR dataset, four of the six configurations (MLP, GAT + metrics, GCN, and GCN + metrics) achieved AUCs of 0.59–0.62, with confidence intervals entirely above chance. The highest AUC was obtained by the GCN. These results indicate no clear advantage of GAT over GCN. In this dataset, metric fusion improved the GAT (F_1: $0.66 \rightarrow 0.70$) but reduced the GCN performance ($0.70 \rightarrow 0.64$).

- ***Explainability*** – Global SHAP importance was computed for all six configurations in each dataset (Figs. 8a – 8c), with MESSIDOR, the full and clean dataset, as the reference. In MESSIDOR, Modularity and Global efficiency are the most influential metrics and Maximum closeness centrality the least, in the GBDT, MLP and GCN + metrics models. The MLP dependence plots (Fig. 10c) show that lower Diameter and higher Modularity and Clustering coefficient push predictions toward higher CVDR risk. This agrees with the group differences in Table 1 and with the only significant within-dataset effects, Diameter and Modularity (Table 4). In RFMiD, diameter is the most influential metric, its high value lowers the predicted risk (Fig. 10a). In ODIR, noisy fundus images, which degrade vascular extraction, prevent the models from learning explainable structure, whereas the clean MESSIDOR dataset yields attributions that agree with the descriptive statistics.

V. CONCLUSION

The graph-based metrics in the present study show partly consistent directional effects for SHAP attributions: high Max degree pushes predictions towards higher risk in all three datasets, and high Diameter towards lower risk in RFMiD and MESSIDOR, whereas Global efficiency and Global clustering coefficient reverse direction in MESSIDOR. In ODIR, SHAP magnitudes are negligible. Direct group comparisons show no CVDR effect in ODIR or RFMiD ($|g| \leq 0.12$; $p_{\text{adj}} \geq 0.658$), matching their near-chance classification performance (AUC 0.46–0.57). MESSIDOR is the only dataset with a measurable signal: CVDR=1 images show smaller Diameter ($g = -0.41$) and higher Modularity ($g = 0.25$), in agreement with their SHAP directions. Four of six models discriminate above chance (AUC $0.54 - 0.62$), with the metrics-only MLP (0.60) close to the best GNN (0.62) as can be observed in Tables 4 and 5.

Future work will focus on enriching node-level representations with per-vessel attributes (e.g., tortuosity) and address these metrics to disease-specific classification tasks. In addition, future studies should incorporate demographic and longitudinal variables to improve early detection of individuals predisposed to cardiovascular abnormalities. Furthermore, the proposed methodology may be extended to other vascular imaging datasets, including microvascular blood network representations.

ABBREVIATIONS:

- AMD - Age Macular Degeneration.
- ARMD - Age-Related Macular Degeneration.
- AUC - Area Under the Curve.
- CAD - Computer-Aieded Diagnosis.
- CI - Confidence Interval.
- CSV - Comma-Separated Values.
- CVDR - Cardiovascular Disease Risk.
- GAT - Graph Attention Network.
- GBDT - Gradient-Boosted Decision Tree.
- GCN - Graph Convolutional Network.
- GLCM - Gray Level Co-occurrence Matrix.
- GLDM - Gray Level Dependence Matrix.
- GLRLM - Gray Level Run Length Matrix.
- GLSZM - Gray Level Size Zone Matrix.
- JPEG - Joint Photographic Experts Group.
- MLP - Multilayer Perceptron.
- NGTDM - Neighborhood Gray Tone Difference Matrix.
- OCTA - Optical Coherence Tomography Angiography.
- p_{adj} - adjusted p-value.
- RGB - Red, Green, and Blue.
- ROC - Receiver Operating Characteristic.

ACKNOWLEDGMENT

The authors acknowledge the use of AI-based tools, such as Perplexity, Gemini and ChatGPT, for assistance in editing, grammar enhancement and spelling checks during the preparation of this manuscript.

REFERENCES

[1] W. Xu, Y.-L. Fu, and D. Zhu, "Resnet and its application to medical image processing: Research progress and challenges," *Computer Methods and Programs in Biomedicine*, vol. 240, p. 107660, 2023. [Online]. Available: https://www.sciencedirect.com/science/article/pii/S0169260723003255

[2] Y. He, "Diving deep: The role of deep learning in medical image analysis, today and tomorrow," in *2024 9th International Conference on Intelligent Informatics and Biomedical Sciences (ICIIBMS)*, vol. 9, 2024, pp. 537–540.

[3] U. Shah and A. Harpale, "A review of deep learning models for computer vision," in *2018 IEEE Punecon*, 2018, pp. 1–6.

[4] P. Costa, A. Galdran, M. I. Meyer, M. Niemeijer, M. Abràmoff, A. M. Mendonça, and A. Campilho, "End-to-end adversarial retinal image synthesis," *IEEE Transactions on Medical Imaging*, vol. 37, no. 3, pp. 781–791, 2018.

[5] Y. Xie and Z.-H. Tan, "A survey of deep learning for complex speech spectrograms," *Speech Communication*, vol. 175, p. 103319, 2025. [Online]. Available: https://www.sciencedirect.com/science/article/pii/S0167639325001347

[6] D. Sookarah and S. Armoogum, "Big data analytics and deep learning in bioinformatics," in *Encyclopedia of Bioinformatics and Computational Biology (Second Edition)*, second edition ed., S. Ranganathan, M. Cannataro, and A. M. Khan, Eds. Oxford: Elsevier, 2025,

This work is licensed under a Creative Commons Attribution 4.0 License. For more information, see https://creativecommons.org/licenses/by/4.0/

This article has been accepted for publication in IEEE Access. This is the author's version which has not been fully edited and
content may change prior to final publication. Citation information: DOI 10.1109/ACCESS.2026.3750743

pp. 638–651. [Online]. Available: https://www.sciencedirect.com/science/article/pii/B9780323955027001482

[7] J. Huang, L. Xiao, J. Yang, and S. Chen, "Using knowledge graphs to enhance the interpretability of clinical decision support model," in *2020 International Conference on Computer Science and Management Technology (ICCSMT)*, 2020, pp. 115–122.

[8] K. Anvesh, B. M. Reshmi, S. Hariharan, H. V. Reddy, M. Krishnamoorthy, V. Kukreja, and S.-Y. Chen, "A novel approach deep learning framework for automatic detection of diseases in retinal fundus images," *CMES - Computer Modeling in Engineering and Sciences*, vol. 143, no. 2, pp. 1485–1517, 2025. [Online]. Available: https://www.sciencedirect.com/science/article/pii/S152614922500147X

[9] A. Durante, A. Mazzapicchi, and M. Baiardo Redaelli, "Systemic and cardiac microvascular dysfunction in hypertension," *International Journal of Molecular Sciences*, vol. 25, no. 24, p. 13294, December 2024.

[10] O. Jorreia, N. Gonçalves, and R. Cortesão, "Graph-based radiomics feature extraction from 2d retina images," *IEEE Access*, vol. 13, pp. 125 359–125 373, 2025.

[11] A. Chaddad and X. Liang, "Stability of radiomic models and strategies to enhance reproducibility," *IEEE Transactions on Radiation and Plasma Medical Sciences*, vol. 8, no. 5, pp. 540–555, 2024.

[12] P. P. Ray, "A review on explainable artificial intelligence in radiomics: State-of-the-art tools, prospective use cases, challenges and future directions," *European Journal of Radiology Artificial Intelligence*, vol. 5, p. 100069, 2026. [Online]. Available: https://www.sciencedirect.com/science/article/pii/S3050577125000672

[13] Y. Han, G. Holste, Y. Ding, A. Tewfik, Y. Peng, and Z. Wang, "Radiomics-guided global-local transformer for weakly supervised pathology localization in chest x-rays," *IEEE Transactions on Medical Imaging*, vol. 42, no. 3, pp. 750–761, 2023.

[14] Y. Liu, J. Liu, and F. Zhang, "Research progress and clinical application of radiomics," in *2021 12th International Symposium on Parallel Architectures, Algorithms and Programming (PAAP)*, 2021, pp. 173–177.

[15] J. Chen, W. He, L. Yang, X. Tao, Q. Li, X. Yang, Y. Mao, S. Liu, D. Liang, X. Liu, H. Zheng, S. Lu, and N. Zhang, "A radiomics-based approach with automated segmentation for identifying symptomatic basilar artery plaques in acute stroke," *Journal of Cardiovascular Magnetic Resonance*, p. 102736, 2026. [Online]. Available: https://www.sciencedirect.com/science/article/pii/S1097664726000542

[16] E. Limkin, R. Sun, L. Dercle, E. Zacharaki, C. Robert, S. Reuzé, A. Schernberg, N. Paragios, E. Deutsch, and C. Ferté, "Promises and challenges for the implementation of computational medical imaging (radiomics) in oncology," *Annals of Oncology*, vol. 28, no. 6, pp. 1191–1206, 2017. [Online]. Available: https://www.sciencedirect.com/science/article/pii/S0923753419324123

[17] F. Mariotti, A. Agostini, A. Borgheresi, M. Marchegiani, A. Zannotti, G. Giacomelli, L. Pierpaoli, E. Tola, E. Galiffa, and A. Giovagnoni, "Insights into radiomics: a comprehensive review for beginners," *Clinical and Translational Oncology*, vol. 27, no. 11, pp. 4091–4102, Nov. 2025.

[18] J.-J. Qiu, J. Yin, W. Qian, J.-H. Liu, Z.-X. Huang, H.-P. Yu, L. Ji, and X.-X. Zeng, "A novel multiresolution-statistical texture analysis architecture: Radiomics-aided diagnosis of pdac based on plain ct images," *IEEE Transactions on Medical Imaging*, vol. 40, no. 1, pp. 12–25, 2021.

[19] C. Laghridat, M. Essalih, and I. Mounir, "The use of image graph in the medical data analyzing," in *2023 IEEE International Conference on Advances in Data-Driven Analytics And Intelligent Systems (ADACIS)*, 2023, pp. 1–5.

[20] H. Zhang, X. Liu, S. Huang, Y. Ma, Y. Yuan, D. Zhang, and L. Zhang, "Graph-level contrastive learning with self-aware and cross-sample topology augmentation for brain disorder diagnosis using rs-fmri," *Neural Networks*, vol. 196, p. 108379, 2026. [Online]. Available: https://www.sciencedirect.com/science/article/pii/S0893608025012602

[21] M. M. Verhulst, P. Lange, A. M. Tuladhar, P. Tewarie, P. C. van Gils, C. van Heugten, J. Bonnes, T. Delnoij, R. Helmich, and J. Hofmeijer, "Brain topology and cognitive outcomes after cardiac arrest: A graph theoretical analysis of fmri data," *NeuroImage: Reports*, vol. 5, no. 1, p. 100244, 2025. [Online]. Available: https://www.sciencedirect.com/science/article/pii/S2666956025000121

[22] Y. Zhao, J. Xie, H. Zhang, Y. Zheng, Y. Zhao, H. Qi, Y. Zhao, P. Su, J. Liu, and Y. Liu, "Retinal vascular network topology reconstruction and artery/vein classification via dominant set clustering," *IEEE Transactions on Medical Imaging*, vol. 39, no. 2, pp. 341–356, 2020.

[23] M. Zare, S. Karimi, M. Shojaeinia, H. Safi, H. Nikkhah, and S. M. Hosseini Imeni, "Opposing end-node and junction-node remodeling patterns in diabetic patients on optical coherence tomography angiography," *Scientific Reports*, vol. 16, no. 1, p. 19146, April 2026.

[24] S. Yu and V. Lakshminarayanan, "Fractal dimension and retinal pathology: A meta-analysis," *Applied Sciences*, vol. 11, no. 5, 2021. [Online]. Available: https://www.mdpi.com/2076-3417/11/5/2376

[25] N. Popovic, M. Radunovic, J. Badnjar, and T. Popovic, "Fractal dimension and lacunarity analysis of retinal microvascular morphology in hypertension and diabetes," *Microvascular Research*, vol. 118, pp. 36–43, 2018. [Online]. Available: https://www.sciencedirect.com/science/article/pii/S0026286218300104

[26] F. Fan, J. He, C. Wang, Z. Zhang, and Q. Zhang, "Multi-scale retinal vessel tortuosity measurement based on wavelet transform," in *2021 11th International Conference on Information Technology in Medicine and Education (ITME)*, 2021, pp. 404–408.

[27] F. C. van der Heide, Y. Zamoum, M. Ounissi, T. T. Berendschot, C. Y. Cheung, M. Koronyo-Hamaoui, L. Schmetterer, J. Chua, T. Peto, I. Lengyel, L. Csincsik, C. Creuzot, L. Arnould, I. Stalmans, E. Trucco, T. Macgillivray, A. P. Khawaja, L. Z. Zhu, P. A. Keane, T. Y. Wong, and D. Milea, "Quantification of retinal microvascular imaging features from fundus photos in ocular and systemic disease: a framework for standardization," *Progress in Retinal and Eye Research*, vol. 112, p. 101461, 2026. [Online]. Available: https://www.sciencedirect.com/science/article/pii/S1350946226000273

[28] T. Buergel, L. Loock, J. Steinfeldt, N. Kronenberg, L. Hoffmann, S. E. Künzel, J. Upmeier zu Belzen, L. Arnoldt, A. P. Khawaja, R. Luben, P. J. Foster, C. Langenberg, U. Landmesser, J. Deanfield, O. Zeitz, A. M. Joussen, M. Pietzner, B. Wild, and R. Eils, "A predictive atlas of disease onset from retinal fundus photographs: a modelling study using data from population-based cohorts," *The Lancet Digital Health*, p. 100962, 2026. [Online]. Available: https://www.sciencedirect.com/science/article/pii/S258975002500144X

[29] N. Popovic, S. Vujosevic, and T. Popovic, "Regional patterns in retinal microvascular network geometry in health and disease," *Scientific Reports*, vol. 9, no. 1, p. 16340, November 2019.

[30] A. A. Kalitzeos, G. Y. Lip, and R. Heitmar, "Retinal vessel tortuosity measures and their applications," *Experimental Eye Research*, vol. 106, pp. 40–46, 2013. [Online]. Available: https://www.sciencedirect.com/science/article/pii/S001448351200320X

[31] L. H. Raffa, E. H. Raffa, Álvaro S. Hervella, L. Ramos, J. Novo, J. Rouco, and M. Ortega, "Computer-assisted evaluation of retinal vessel tortuosity in children with sickle cell disease without retinopathy," *Microvascular Research*, vol. 157, p. 104752, 2025. [Online]. Available: https://www.sciencedirect.com/science/article/pii/S0026286224001018

[32] D. Chen, L. Yao, L. Bai, E. R. Hancock, and L. Zhang, "Motif-aware brain functional connectivity network analysis for cognitive disorder diagnosis," *Pattern Recognition*, vol. 179, p. 113655, 2026. [Online]. Available: https://www.sciencedirect.com/science/article/pii/S0031320326006205

[33] C.-L. Tsai, P.-L. Lee, C.-S. Liang, Y.-K. Lin, G.-Y. Lin, C.-K. Tsai, Y.-C. Hsu, C.-P. Lin, K.-H. Chou, and F.-C. Yang, "Disrupted brain connectivity patterns in early-to-middle-aged adults with subjective memory complaints: A longitudinal resting-state functional magnetic resonance imaging study," *Psychiatry Research*, vol. 353, p. 116732, 2025. [Online]. Available: https://www.sciencedirect.com/science/article/pii/S0165178125003774

[34] J. De, L. Cheng, X. Zhang, F. Lin, H. Li, K. H. Ong, W. Yu, Y. Yu, and S. Ahmed, "A graph-theoretical approach for tracing filamentary structures in neuronal and retinal images," *IEEE Transactions on Medical Imaging*, vol. 35, no. 1, pp. 257–272, 2016.

[35] Y. Bo, T. Zhou, Z. Li, H. Zhang, and L. Shao, "Contrastive graph modeling for cross-domain few-shot medical image segmentation," *IEEE Transactions on Medical Imaging*, vol. 45, no. 5, pp. 2173–2186, 2026.

[36] Y. Li, X. Zhang, J. Nie, G. Zhang, R. Fang, X. Xu, Z. Wu, D. Hu, L. Wang, H. Zhang, W. Lin, and G. Li, "Brain connectivity based graph convolutional networks and its application to infant age prediction," *IEEE Transactions on Medical Imaging*, vol. 41, no. 10, pp. 2764–2776, 2022.

[37] M. Rubinov and O. Sporns, "Complex network measures of brain connectivity: Uses and interpretations," *NeuroImage*, vol. 52, no. 3, pp. 1059–1069, 2010, computational Models of the Brain. [Online]. Available: https://www.sciencedirect.com/science/article/pii/S105381190901074X

[38] Q. Cai, S. Alam, and J. Liu, "On the robustness of complex systems with multipartitivity structures under node attacks," *IEEE Transactions on Control of Network Systems*, vol. 7, no. 1, pp. 106–117, 2020.

[39] K. Yang, J. Li, M. Liu, T. Lei, X. Xu, H. Wu, J. Cao, and G. Qi, "Complex

This work is licensed under a Creative Commons Attribution 4.0 License. For more information, see https://creativecommons.org/licenses/by/4.0/

This article has been accepted for publication in IEEE Access. This is the author's version which has not been fully edited and
content may change prior to final publication. Citation information: DOI 10.1109/ACCESS.2026.3750743

systems and network science: a survey," *Journal of Systems Engineering and Electronics*, vol. 34, no. 3, pp. 543–573, 2023.

[40] L. Zhao, "Complex network modeling analysis of social and cultural communication node paths," in *2022 6th International Conference on Trends in Electronics and Informatics (ICOEI)*, 2022, pp. 647–650.

[41] B. Ristevski, S. Savoska, and Z. Savoski, "Using graph databases for portraying and analysing biological and biomedical networks," in *2022 8th International Conference on Control, Decision and Information Technologies (CoDIT)*, vol. 1, 2022, pp. 565–568.

[42] G. Lin, S. Liu, and B. Zhao, "Mapping the energy internet physical and cyber system into complex networks model," in *2022 7th Asia Conference on Power and Electrical Engineering (ACPEE)*, 2022, pp. 152–156.

[43] P. Boldi, "The emergence of hypergraphs in complex system analysis," in *2023 IEEE 9th International Conference on Collaboration and Internet Computing (CIC)*, 2023, pp. 1–7.

[44] A. Arakala, S. Davis, H. Hao, and K. Horadam, "Value of graph topology in vascular biometrics," *IET Biometrics*, vol. 6, no. 2, pp. 117–125, mar 2017.

[45] M. Shumal, M. Saghafian, E. Shirani, and M. Nili-AhmadAbadi, "Association of murray's law with atherosclerosis risk: Numerical validation of a general scaling law of arterial tree," *Computers in Biology and Medicine*, vol. 186, p. 109741, 2025. [Online]. Available: https://www.sciencedirect.com/science/article/pii/S0010482525000915

[46] M. E. J. Newman, "The structure and function of complex networks," *SIAM Review*, vol. 45, no. 2, pp. 167–256, 2003. [Online]. Available: https://doi.org/10.1137/S003614450342480

[47] L. Li, M. Verma, Y. Nakashima, R. Kawasaki, and H. Nagahara, "Joint learning of vessel segmentation and artery/vein classification with post-processing," in *Proceedings of the Medical Imaging with Deep Learning (MIDL)*. PMLR, 2020, pp. 1–10. [Online]. Available: https://proceedings.mlr.press/v121/li20a.html

[48] S. Pachade, P. Porwal, D. Thulkar, M. Kokare, G. Deshmukh, V. Sahasrabuddhe, L. Giancardo, G. Quellec, and F. Mériaudeau, "Retinal fundus multi-disease image dataset (rfmid): A dataset for multi-disease detection research," *Data*, vol. 6, no. 2, 2021. [Online]. Available: https://www.mdpi.com/2306-5729/6/2/14

[49] L. A. MVD), "Retinal disease classification," https://www.kaggle.com/datasets/andrewmvd/retinal-disease-classification, 2020, [Online; accessed Feb. 20, 2026].

[50] B. K. Triwijoyo, A. Adil, D. S. Chani Saputri, and A. Anggrawan, "Morphology approach for segmentation of blood vessels in retinal images," in *2023 6th International Conference of Computer and Informatics Engineering (IC2IE)*, 2023, pp. 346–350.

[51] S. Jiang, X. Kui, X. Bao, Q. Li, Z. Hu, and B. Zou, "Rmvim-net: Residual multi-path vision mamba with graph interaction attention for medical image segmentation," *Knowledge-Based Systems*, vol. 336, p. 115326, 2026. [Online]. Available: https://www.sciencedirect.com/science/article/pii/S0950705126000705

[52] H. Hao, W. Wang, Y. Chen, Q. Dingl, F. Hao, H. Zhang, and J. Bai, "Interactive medical image segmentation in various imaging modalities: Current status and challenges," in *2025 28th International Conference on Computer Supported Cooperative Work in Design (CSCWD)*, 2025, pp. 50–55.

[53] Y. Xu and Y. Fan, "Dual-channel asymmetric convolutional neural network for an efficient retinal blood vessel segmentation in eye fundus images," *Biocybernetics and Biomedical Engineering*, vol. 42, no. 2, pp. 695–706, 2022. [Online]. Available: https://www.sciencedirect.com/science/article/pii/S0208521622000419

[54] Y. Zhou, M. Xu, Y. Hu, H. Lin, J. Jacob, P. A. Keane, and D. C. Alexander, "Learning to address intra-segment misclassification in retinal imaging," in *Medical Image Computing and Computer Assisted Intervention – MICCAI 2021*, M. de Bruijne, P. C. Cattin, S. Cotin, N. Padoy, S. Speidel, Y. Zheng, and C. Essert, Eds. Cham: Springer International Publishing, 2021, pp. 482–492.

[55] D. Feng, H. Zhang, W. Zhang, H. Xie, Y. Zhang, and X. Song, "Pipeline network robustness analysis with complex network theory," *Journal of Pipeline Science and Engineering*, p. 100420, 2025. [Online]. Available: https://www.sciencedirect.com/science/article/pii/S2667143325001672

[56] H. Liao, M. S. Mariani, M. Medo, Y.-C. Zhang, and M.-Y. Zhou, "Ranking in evolving complex networks," *Physics Reports*, vol. 689, pp. 1–54, 2017, ranking in evolving complex networks. [Online]. Available: https://www.sciencedirect.com/science/article/pii/S0370157317300935

[57] P. Shiguihara-Juárez and N. Murrugarra-Llerena, "A gaussian model for feature selection in protein fold recognition," in *2018 IEEE Sciences and Humanities International Research Conference (SHIRCON)*, 2018, pp. 1–3.

[58] Y. Deng, M. Eden, and S. Cremaschi, "A gaussian process embedded feature selection method based on automatic relevance determination," *Computers & Chemical Engineering*, vol. 191, p. 108852, 2024. [Online]. Available: https://www.sciencedirect.com/science/article/pii/S0098135424002709

[59] A. Hoayek and D. Rullière, "Assessing clustering methods using shannon's entropy," *Information Sciences*, vol. 689, p. 121510, 2025. [Online]. Available: https://www.sciencedirect.com/science/article/pii/S0020025524014245

[60] B. Archana and K. Kalirajan, "A survey of medical image processing and its applications," in *2022 4th International Conference on Inventive Research in Computing Applications (ICIRCA)*, 2022, pp. 1541–1546.

[61] B. Xin, C. Xu, L. Wang, T. Dong, C. Zheng, and X. Wang, "Integrative clustering and supervised feature selection for clinical applications," in *2018 15th International Conference on Control, Automation, Robotics and Vision (ICARCV)*, 2018, pp. 1316–1320.

[62] J. Arredondo Montero, "A structured guide to univariate test selection based on normality, variance homogeneity, and graphical data exploration," *Journal of Surgical Research*, vol. 318, pp. 230–240, 2026. [Online]. Available: https://www.sciencedirect.com/science/article/pii/S002248042500695X

[63] C. E. Agbangba, E. Sacla Aide, H. Honfo, and R. Glèlè Kakai, "On the use of post-hoc tests in environmental and biological sciences: A critical review," *Heliyon*, vol. 10, no. 3, p. e25131, 2024. [Online]. Available: https://www.sciencedirect.com/science/article/pii/S2405844024011629

[64] P. Marfo and G. Okyere, "The accuracy of effect-size estimates under normals and contaminated normals in meta-analysis," *Heliyon*, vol. 5, no. 6, p. e01838, 2019. [Online]. Available: https://www.sciencedirect.com/science/article/pii/S2405844018326239

[65] S. M. Gbashi, O. O. Olatunji, P. A. Adedeji, and N. Madushele, "An explainable ai approach using shapley additive explanations for feature selection in vibration-based fault diagnostics of wind turbine gearbox," in *2024 IEEE 5th International Conference on Electro-Computing Technologies for Humanity (NIGERCON)*, 2024, pp. 1–5.

[66] D. K. V V, S. Sreesankar, K. Dinesan, P. B. Nair, and L. R. Deepthi, "Analyzing gnn models for community detection using graph embeddings: A comparative study," in *2024 15th International Conference on Computing Communication and Networking Technologies (ICCCNT)*, 2024, pp. 1–8.

[67] G. Theis Marchan, T. O. Balogun, K. Territo, D. Das, T. Olayiwola, R. Kumar, and J. A. Romagnoli, "Toward harnessing ai for surfactant chemistry: Prediction of critical micelle concentration," *Computational Materials Science*, vol. 265, p. 114548, 2026. [Online]. Available: https://www.sciencedirect.com/science/article/pii/S0927025626000674

[68] F. Mostofi, V. Toğan, and O. B. Tokdemir, "Spatio-temporal data fusion for adversarially resilient graph neural networks in construction progress management," *Advanced Engineering Informatics*, vol. 69, p. 104019, 2026. [Online]. Available: https://www.sciencedirect.com/science/article/pii/S1474034625009127

[69] J. Inbakumar, J. P. S, and C. Illakiyavarshini, "Eye disease detection using gcn, gat, and graphsage," in *2025 2nd International Conference on Artificial Intelligence for Innovations in Healthcare Industries (ICAIIHI)*, 2025, pp. 1–6.

[70] Y. Li, N. Zhao, S. Liu, Y. Wu, J. Nie, and J. Li, "Demand response potential prediction based on gat considering spatial correlation," in *2025 2nd International Conference on Smart Grid and Artificial Intelligence (SGAI)*, 2025, pp. 977–981.

[71] S. Ben Atitallah, C. Ben Rabah, M. Driss, W. Boulila, and A. Koubaa, "Self-supervised learning for graph-structured data in healthcare applications: A comprehensive review," *Computers in Biology and Medicine*, vol. 188, p. 109874, 2025. [Online]. Available: https://www.sciencedirect.com/science/article/pii/S0010482525002252

This work is licensed under a Creative Commons Attribution 4.0 License. For more information, see https://creativecommons.org/licenses/by/4.0/

This article has been accepted for publication in IEEE Access. This is the author's version which has not been fully edited and
content may change prior to final publication. Citation information: DOI 10.1109/ACCESS.2026.3750743



OFÉLIO JORREIA is PhD student in Electrical Engineering and Intelligent Systems – Institute of Systems and Robotics at University of Coimbra.

He holds a degree in Computer Science from Pedagogical University of Mozambique and a Master's degree in Technologies, Systems, and Communication Networks from Polytechnic University of Valencia, Spain. He collaborated with the research group at the Instituto de Tecnologías y Aplicaciones Multimedia de València, focusing on the early diagnosis of brain diseases such as Alzheimer's and schizophrenia through computational intelligence applied to functional magnetic resonance imaging (fMRI). He has also served as a lecturer at Pedagogical University and Rovuma University, both in Mozambique.



NUNO GONÇALVES is researcher at the Institute of Systems and Robotics – University of Coimbra and Tenured Assistant Professor at the Dept. of Electrical and Computers Engineering of the University of Coimbra.

He received his MsC and PhD degrees in 2002 and 2008, respectively from the University of Coimbra. His main research areas are computer vision, biometrics, machine-readable codes, security printing, computer graphics and machine learning, with special emphasis to biometrics and steganography for ID and travel documents.

He has scientific publications in the following topics: visual coding (machine-readable codes), steganography, object recognition, facial recognition and diagnosis, biometrics, documents security, augmented and virtual reality, reflections for image rendering, light field cameras, omnidirectional vision, non-central cameras, calibration, optics, camera models, motion estimation, pose estimation, web information systems, sports vision, legged robotics, amongst others.

He was the Principal Investigator of a closed project, funded by the Portuguese Science and Technology Foundation, in non-central camera models for computer graphics and computer-aided surgery and he is currently Scientific Coordinator of several projects with the industry (funded by the INCM – Portuguese Mint and Official Printing Office) in the area of security elements involving: biometrics, machine readable codes (with some applications in virtual and augmented reality), security unique marks in printing labels, security unique marks in assay contrasts in artifacts of precious metals and processing of human faces in 3D by using several types of cameras. He is inventor of six patents. Since 2018 he is also Innovation Manager in INCM.



RUI CORTESÃO received the B.Sc. ("Licenciatura") degree in electrical engineering, the M.Sc. degree in systems and automation, and the Ph.D. degree in control and instrumentation from the University of Coimbra, Coimbra, Portugal, in 1994, 1997, and 2003, respectively. He was a Visiting Researcher at the German Aerospace Center-DLR, Oberpfaffenhofen, Germany, during 1998–2003, where he did his Ph.D. work at Stanford University, Stanford, CA, USA, in 2002, at LIRMM-CNRS, Montpellier, France, in 2004, 2006, and 2008, at Barrett Technologies, Boston, MA, USA, in 2007, and at Trinity College, Dublin, Ireland, 2018, having worked on surgical robotics, haptic tele-manipulation, compliant motion control, data fusion and human-robot skill transfer. He is currently Professor with the University of Coimbra, Head of the Medical Robotics Group at the Institute of Systems and Robotics (ISR-UC), and Director of the technology transfer lab IPN-LAS.

This work is licensed under a Creative Commons Attribution 4.0 License. For more information, see https://creativecommons.org/licenses/by/4.0/